Title

Electrostatics of Nanoparticle-Wall Interactions within Nanochannels: Role of Double-Layer Structure and Ion-Ion Correlations.

Journal

ACS omega, 3(9)

ISSN

2470-1343

Authors

Sidhu, Inderbir S
Frischknecht, Amalie L
Atzberger, Paul J

Publication Date

2018-09-01

DOI

10.1021/acsomega.8b01393

Peer reviewed

ACS OMEGA

Article

Cite This: ACS Omega 2018, 3, 11340−11353

http://pubs.acs.org/journal/acsodf

Electrostatics of Nanoparticle−Wall Interactions within Nanochannels: Role of Double-Layer Structure and Ion−Ion Correlations

Inderbir S. Sidhu,[†] Amalie L. Frischknecht,[‡] and Paul J. Atzberger*[,†]

[†]Department of Mathematics and Department of Mechanical Engineering, University of California at Santa Barbara, Santa Barbara, California 93106, United States

[‡]Center for Integrated Nanotechnologies, Sandia National Laboratories, Albuquerque, New Mexico 87185, United States

Supporting Information

ABSTRACT: We perform computational investigations of the electrolyte-mediated interactions of charged nanoparticles with the walls of nanochannels. We investigate the role of discrete ion effects, valence, and electrolyte strength on nanoparticle−wall interactions. We find for some of the multivalent charge regimes that the like-charged nanoparticles and walls can have attractive interactions. We study in detail these interactions and the free-energy profile for the nanoparticle−wall separation. We find there are energy barriers and energy minima giving preferred nanoparticle locations in the channel near the center and at a distance near to but separated from the channel walls. We characterize contributions from surface overcharging, condensed layers, and overlap of ion double layers. We perform our investigations using coarse-grained particle-level simulations with Brownian dynamics, classical density functional theory, and the mean-field Poisson−Boltzmann theory. We discuss the implications of our results for phenomena in nanoscale devices.

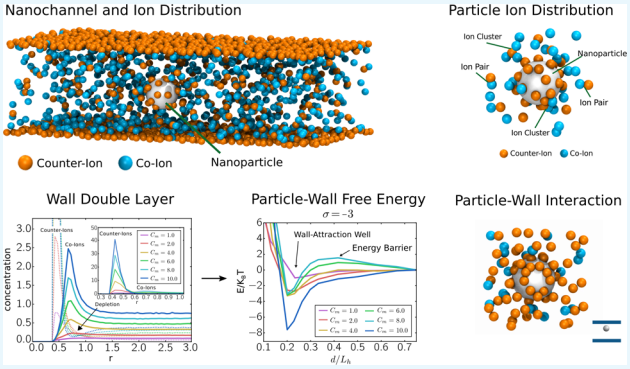

1. INTRODUCTION

In many microscale and nanoscale systems, electrolytes play a central role in collective interactions, equilibrium phase behaviors, and kinetics.[1−3] This includes transitions in the stability of colloidal suspensions,[4−6] electrophoretic separation and detection in fluidic devices,[1−3,7−9] and biomolecular interactions.[10−12] Confinement of electrolytes and charged objects between charged walls presents additional effects often resulting in rich phenomena that are particularly important in nanoscale devices.[1,7] This owes in part to such features as the thickness of ionic layers becoming comparable to other length scales in the system.[2,13−15]

For sufficiently charged multivalent systems, additional phenomena can arise, as observed in experiments and predicted by theory.[16−20] This includes the formation of condensed ion layers on surfaces, overcharging of walls and particles, and attractions between like-charged objects.[17,21,22] These effects have formed the basis for understanding phenomena such as DNA condensation,[23−27] colloidal stability,[6,17,28] and attraction of like-charged plates.[16,18,19]

There has been significant related experimental work done to address for applications the important problem of characterizing the size and charge features of nanoparticles and their interactions within nanoscale systems and devices.[8,29,30] In the work of Krishnan et al.,[30] detailed experimental investigations were made of a nanoscale device with a geometry that generates electrostatically local energy wells that transiently trap nanoparticles, allowing for characterizations of particle size and charge. In Tagliazucchi et al.,[29] further investigations are discussed concerning the importance of charged nanoparticle interactions with nanopores and nanochannels going beyond effects captured by the Poisson−Nernst−Planck and Poisson−Boltzmann (PB) theory.

Here, we investigate the behavior of charged nanoparticles confined within nanochannels filled with electrolyte, using coarse-grained molecular-level simulations using Brownian dynamics (BD) and classical density functional theory (cDFT). We also make comparisons with predictions from the mean-field Poisson−Boltzmann (PB) theory. We investigate the interactions between a charged nanoparticle and the nanochannel wall as the electrolyte concentration and particle charge are varied. We focus particularly on the case of divalent counterions and strongly charged surfaces. There have been relatively few detailed studies of charged nanoparticles within charged nanochannels going beyond mean-field PB theory to take into account effects of discrete ions, ion sterics, ion−ion

Received: June 20, 2018
Accepted: September 6, 2018
Published: September 18, 2018

DOI: 10.1021/acsomega.8b01393
ACS Omega 2018, 3, 11340−11353

correlations, and the role of particle-channel geometry. Some notable previous work going beyond PB includes[31] who developed cDFT approaches to investigate charged spherical nanoparticles in nanochannels with weakly charged walls. To our knowledge, our work is the first to investigate in detail the strongly charged regime in this geometry and to investigate comparisons between the predictions of a particle-based model, cDFT, and mean-field PB theory for nanochannels.

In our investigations, we find that in some charge regimes, the free energy of the particle as a function of its position within the channel can develop significant energy minima in preferred locations near the channel center and near to, but separated from, the channel wall. In some regimes, we find these preferred locations (energy minima) can become separated by significant energy barriers. Motivated by nanofluidic devices, our results indicate that nanoparticles could exhibit interesting bimodalities switching from long dwell times in locations near the channel wall to locations near the channel center. The ways this affects transport could have implications for experimental protocols and design of devices for processes such as capillary electrophoresis used in fluidics for separations and detection.[1,2,7,32−34]

We investigate the origin of the free-energy profile for the location of the nanoparticle within the channel by using BD simulations. We characterize at the coarse-grained molecular level the ion−ion correlations and the surface overcharging and condensed ionic layers that form near the nanoparticle surface and channel wall. We further make comparisons with results from classical density functional theory (cDFT). We find the cDFT make predictions consistent with our molecular-level results but in the most strongly charged regimes with significant underestimation of the strength of effects such as the free-energy well depth. For the free-energy profile of the confined particle, the combined simulation and cDFT results demonstrate the significant roles played by ion−ion correlations and overcharging at both the charged walls and nanoparticle surface. We also show for the strongly charged regimes considered that a mean-field theory such as the Poisson−Boltzmann theory is not adequate in predicting system behaviors, highlighting the importance of accounting for ion−ion correlations and other discrete effects.

We introduce our BD simulations for the electrolyte and nanoparticle in Section 2.1. We introduce our cDFT description of the nanochannel system in Section 2.2. We present the results of our calculations, including the counterion and coion densities, nanoparticle free energy, and ion−ion correlation functions in Section 3. We discuss our findings and related phenomena observed within nanochannels in Section 4. Additional information on the computational methods developed and simulation protocols are discussed in the Supporting Information.

2. METHODS

2.1. Brownian Dynamics Simulations. We consider nanoparticles confined within a nanochannel having a slit-like geometry. The walls of the channel are two like-charged parallel plates. We consider electrolytes consisting of both counterions and coions, using a coarse-grained model related to the restricted primitive model.[35−37] The discrete ion−ion interactions are taken into account within a continuous dielectric medium. A snapshot of the system is shown in Figure 1. Additional details on the electrostatics of channels are presented in Section S.1.

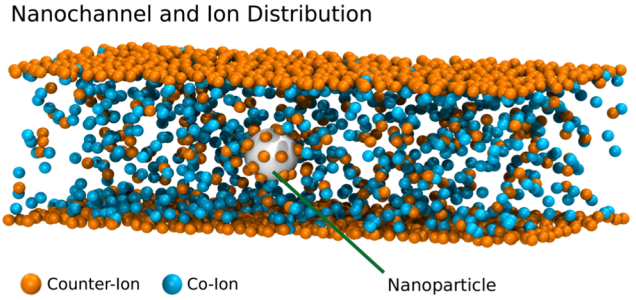

Figure 1. Shown is a cut-away view of the electrolyte and nanoparticle corresponding to counterions with +2 charge (orange) and coions with −1 charge (blue). Strong correlations are exhibited, where counterions and coions form clusters and chains throughout the electrolyte and condensed layers near the walls and nanoparticle surface. For clarity, the channel walls are not shown. The shown configuration of ions and colloid corresponds to the parameters $\sigma = -6$ and $C_m = 8$ defined in Section 2.1.1.

We model the finite size of the ions and the excluded volume of the nanoparticle using the Weeks−Chandler−Andersen interaction potential[38]

$$\phi_{\mathrm{wca}}(r) = \begin{cases} 4\epsilon\left[(b/r)^{12} - (b/r)^{6} + \frac{1}{4}\right], & r \le r_c \\ 0, & r > r_c \end{cases} \quad (1)$$

r is the distance between the center of mass of the two particles. For a particle with steric radius b, we have $r_c = 2^{1/6}\cdot b$. This ensures a purely repulsive interaction between particles.[38] We also include for the particle and wall a steric interaction that enforces no penetration of ions through the walls. We treat the walls as a smooth continuum and use a Lennard-Jones (LJ) 9-3 potential truncated at $r_c^{[w]}$ to only retain the repulsive part

$$\phi_{\mathrm{lj93}}(r) = \epsilon\left[\frac{2}{15}(b/r)^{9} - (b/r)^{3}\right] \quad (2)$$

Here, r denotes the nearest distance between a particle and the wall. Given the frequency of ion−wall interactions, we found the 9-3 LJ potential offers some numerical advantages over the 12-6 LJ potential while still preserving well approximate hard-wall interactions, allowing for significantly larger time steps when sampling the ion configurations. Electrostatic interactions between ions and/or the nanoparticles of charge q_1 and q_2 are given by the Coulomb interaction

$$\phi_{\mathrm{coul}}(r) = \frac{q_1 q_2}{4\pi\epsilon_0\epsilon r} \quad (3)$$

where ϵ is the dielectric constant of the background medium and we use SI units. To account for the surface charge density σ of the nanoparticle, we use Gauss's law,[39] allowing us to use a point charge Q_0 at the center of mass with $Q_0 = 4\pi R^2\sigma$, where R is the radius of the particle.

To handle the long-range Coulumb interactions we use the particle−particle particle−mesh (PPPM) approach,[40,41] as implemented in LAMMPS.[42] For the nanochannel with slit geometry, we use a variant of the PPPM method that uses periodic boundary conditions in the xy directions.[43] This method has been extended to allow the simulated system to have a net charge within the slab interior.[44] We use in our simulations the approach of Ballenegger et al.,[44] as

DOI: 10.1021/acsomega.8b01393
ACS Omega 2018, 3, 11340−11353

Table 1. Parameter Values for the Nanochannel Model[a]

parameter	value	parameter	value
nanochannel width (z), l_z	6 nm	nanochannel length (x, y), l_x, l_y	18 nm
wall surface charge, σ_w^*	$-0.72e/\text{nm}^2$	wall steric parameter lj93, b_w	0.5 nm
wall cutoff parameter lj93, $r_c^{[w]}$	0.425 nm	wall energy lj93, ϵ_w	2.27×10^7 amu nm^2/ns^2
particle surface charge, $\tilde{\sigma}$	$-3e/\text{nm}^2$	particle radius, R	0.75 nm
particle mass, m_0	6.20×10^3 amu	temperature, T	300 K
thermal energy, k_BT	2.50×10^6 amu nm^2/ns^2	solvent mass density, ρ	6.02×10^2 amu/nm^3
solvent viscosity, μ	5.36×10^5 amu/(nm ns)	solvent relative permittivity, ϵ_r	80.1
counterion radius, b_-	0.116 nm	coion radius, b_+	0.116 nm
counterion charge, q_-	$-1e$	coion charge, q_+	$+2e$
counterion effective mass, m_-	2.3×10^1 amu	coion effective mass, m_+	2.3×10^1 amu
reference-ion concentration, $\bar{c}_-$	0.214 M	reference-ion concentration, $\bar{c}_+$	0.128 M
wall LJ cutoff, $r_c^{[w]}$	0.425 nm	coulombic cutoff, $r_c^{[c]}$	6 nm
Langevin time step, Δt	1.0×10^{-5} ns	Langevin drag, γ	$6\pi\mu R$
Langevin equilibration time, τ_e	0.5 ns		

[a]We use by default these values unless specified otherwise.

implemented in LAMMPS. Our overall system is electrically neutral with the electrostatics of the channel walls to be interpreted using our approach discussed in Section S.1.

In simulations, to calculate the potential of mean force, we use a harmonic potential to hold the nanoparticle at a given location by

$$\phi_{\text{target}}(\mathbf{x}) = \frac{k}{2}|\mathbf{x} - \mathbf{x}_0|^2 \tag{4}$$

where $\mathbf{x}_0$ is the target location for the nanoparticle location $\mathbf{x}$. The total potential energy associated with a configuration of the nanochannel system including the counterions, coions, and nanoparticle is given by

$$\Phi[\mathbf{X}] = \Phi_{\text{coul}}[\mathbf{X}] + \Phi_{\text{sterics}}[\mathbf{X}] + \Phi_{\text{target}}[\mathbf{X}] \tag{5}$$

where we represent the configuration of nanoparticle and ions by the composite vector $\mathbf{X} = [\mathbf{X}_{\text{nanoparticle}}, \mathbf{X}_{\text{ions}}]^T$. To sample equilibrium configurations, we use Brownian dynamics (BD) based on the Langevin equations[45]

$$m\frac{d\mathbf{V}}{dt} = -\gamma\mathbf{V} - \nabla\Phi[\mathbf{X}] + \mathbf{F}_{\text{thm}} \tag{6}$$

The $d\mathbf{X}/dt = \mathbf{V}$ gives the collective particle velocity, m the particle mass, γ the solvent drag, $\Phi(\mathbf{X})$ is the potential energy of the collective configuration $\mathbf{X}$ of particles, and $\mathbf{F}_{\text{thm}}$ is a stochastic force modeling the thermal fluctuations of the system. We use for $\mathbf{F}_{\text{thm}}$ a Gaussian driving force with mean zero and covariance $\langle \mathbf{F}_{\text{thm}}(s)\mathbf{F}_{\text{thm}}^T(t)\rangle = 2k_BT\gamma\delta(t-s)$.[45] For the time integration, we use a stochastic velocity-Verlet method implemented within LAMMPS.[42,46] All BD simulations are performed in LAMMPS, with parameter values as given in Table 1.

We remark that throughout this paper we use BD to probe only equilibrium properties of the system. The BD simulations were equilibrated from random initial conditions over times long enough for the ions to diffuse at least two times across the diameter of the nanochannel. We then collected statistics on trajectories in which the ions diffused at least five times across the nanochannel diameter.

2.1.1. Model Parameters. We investigate the structure of the double layer when varying the strength of the charge of the nanoparticle and the ion concentrations. We characterize the charge of the negatively charged nanoparticle Q_{particle} in terms of its surface charge density $\tilde{\sigma}$, where $Q_{\text{particle}} = 4\pi R^2\tilde{\sigma}$. We performed simulations for nanoparticles with surface charge densities of $\tilde{\sigma} = -1$, -3, and $-6e/\text{nm}^2$. In presenting our results throughout, we introduce the nondimensional surface charge quantity $\sigma = \tilde{\sigma}/\tilde{\sigma}_0$, where $\tilde{\sigma}_0 = +1e/\text{nm}^2$. This gives the nondimensional surface charge cases $\sigma = -1$, -3, and -6 on which we report throughout. We mostly focus on divalent cations with $q_+ = 2e$ and monovalent anions with $q_- = -1e$. We take as a reference concentration for the counterions $\bar{c}_+ = 0.128$ M and for the coions $\bar{c}_- = 0.214$ M, expressed in molar units. These values were determined from exploratory cDFT calculations of pure channels without nanoparticle to find a physical regime indicative of interesting double-layer structures to explore further with the particle-based model. The other ion concentrations we consider are a multiple C_m of these baseline reference concentrations. For example, $C_m = 10$ corresponds to a counterion concentration $c_+ = C_m\bar{c}_+ = 1.28$ M and a coion concentration $c_- = C_m\bar{c}_- = 2.14$ M. The simulations are performed with a fixed number of ions, with an excess of counterions, so that the bulk electrolyte solution is not neutral. The excess counterions (cations) lead to an effective negative charge on the nanochannel walls, given by the condition of overall electric neutrality

$$q_-N_- + q_+N_+ + Q_{\text{particle}} + 2Q_{\text{wall}} = 0 \tag{7}$$

Here, $N_- = Vc_-$ and $N_+ = Vc_+$ denote the number of ions in the unit cell where V is the channel volume. Q_{wall} is the charge on each wall in the unit cell. For a given fixed concentration of coions and counterions, the effective surface charge of the wall is obtained from electric neutrality by solving for Q_{wall} in eq 7. The wall surface charge density for each system simulated is given in units of e/nm^2 in Table 2. The wall charge density increases with increasing ion concentration. Additionally, the wall surface charge densities vary slightly depending on the nanoparticle charge, since we have a fixed number of ions in the channel.

In the regimes we consider, the electrostatic interactions vary in strength. We can characterize the strength of the interactions by the electrostatic coupling constant[47] given by

$$g \equiv 2\pi q^3 l_B^2 \sigma \tag{8}$$

Here, $q = 2e$ is the charge of the divalent counterions and σ is the charge density of either the nanoparticle or the channel walls. With the Bjerrum length l_B, the distance at which the electrostatic interaction energy is comparable to the thermal

DOI: 10.1021/acsomega.8b01393
ACS Omega 2018, 3, 11340−11353

Table 2. Wall Surface Charge Density (Units Are e/nm)[a]

	$\sigma = -1$	$\sigma = -3$	$\sigma = -6$
$C_m = 1$	−0.74	−0.72	−0.68
$C_m = 2$	−1.49	−1.46	−1.43
$C_m = 4$	−2.98	−2.96	−2.93
$C_m = 6$	−4.48	−4.46	−4.43
$C_m = 8$	−5.98	−5.95	−5.92
$C_m = 10$	−7.47	−7.45	−7.42

[a]For the different regimes considered, we give the implicit surface charge density that arises from electric neutrality given by the condition in eq 7.

energy k_BT, is $l_B \equiv e^2/4\pi kT\epsilon\epsilon_0$. In our systems with divalent cations, the electrostatic coupling constant ranges from $g \approx 17$ for the least charged system up to $g \approx 188$ for the most strongly charged system. Previous studies of electrolytes near flat surfaces[47] have shown that the counterion density profiles agree with the PB theory for $g \approx 1$, the profiles show clear deviation from PB theory for $g = 10$ and 100, and they show good agreement with the strong-coupling limit for $g = 10^4$; see ref 47. Previous simulations of highly charged spheres explored coupling constants ranging from $g = 26$ up to 615 and found attraction between like-charged spheres.[48−50] We therefore expect our simulations to be in the intermediate regime between weak and strong coupling.

2.2. Classical Density Functional Theory (cDFT). In the classical density functional theory (cDFT) calculations, we model the ions as interacting charged hard spheres with diameters d_α and charges q_α in a background continuum dielectric medium to represent the solvent. The nanoparticle is a larger hard sphere of radius R and surface charge density σ. The ions are treated as mobile fluid species, whereas the nanoparticle has a fixed spatial location. We account for the steric interactions between the ions and nanoparticle using a hard-sphere interaction $V(r) = \infty$ for $r < R$, where r is the distance between the ion and the center of the nanoparticle. In addition, we add a smooth truncated potential based on the Lennard-Jones (LJ) interaction to the surface of the nanoparticle

$$V_\alpha^{\mathrm{mLJ}}(r') = 4\epsilon_m\left[\left(\frac{R}{r'}\right)^{12} - \left(\frac{R}{r'}\right)^{6}\right] \tag{9}$$

where R is the radius of the nanoparticle and r' is the distance between the ion and the surface of the nanoparticle. We truncate and shift this potential to obtain

$$V_\alpha^{\mathrm{m}}(r') = V_\alpha^{\mathrm{mLJ}}(r') - V_\alpha^{\mathrm{mLJ}}(r'_c),\ r' < r'_c \tag{10}$$

with $V_\alpha^{\mathrm{m}}(r') = 0$ for $r' > r'_c$, at large distances from the nanoparticle. In our notation, the subscript α refers to the index of the particular ion species and the mLJ and m refer to the modified Lennard-Jones potentials. This repulsive potential serves to smooth the surface of the nanoparticle to reduce mesh-size effects in our discretized cDFT. We used $\epsilon_m = 0.5k_BT$ and $\sigma_m = d$ (where d is the ion diameter) for all calculations. The channel boundaries are modeled as hard walls with the interaction potential for the ions

$$V_\alpha^{\mathrm{w}}(z) = \begin{cases} \infty, & \text{ions outside the channel} \\ 0, & \text{ions inside the channel} \end{cases} \tag{11}$$

We use a version of cDFT that follows closely the work of Oleksy and Hansen[51] and is very similar to that of Henderson et al.[52] We formulate the cDFT in an open ensemble, specified by the temperature T, the total volume V, and the chemical potentials μ_α of all fluid species in the system. We discuss the relation of these parameters to those used in the BD simulations in Section 2.2.1.

The grand free energy of the system is given as a functional of the ion densities $\rho_\alpha(\mathbf{r})$

$$\Omega[\rho_\alpha(\mathbf{r})] = \sum_\alpha F[\rho_\alpha(\mathbf{r})] \tag{12}$$

$$-\sum_\alpha \int d\mathbf{r}(\mu_\alpha - V_\alpha(\mathbf{r}))\rho_\alpha(\mathbf{r}) \tag{13}$$

For notational convenience, it is to be understood that $\Omega[\rho_\alpha(\mathbf{r})]$ depends on all of the density fields $\{\rho_\alpha\}$ collectively. Here, $F[\rho_\alpha(\mathbf{r})]$ is the intrinsic Helmholtz free energy of the system. $V_\alpha(\mathbf{r}) = V + V^{\mathrm{m}} + V^{\mathrm{w}}$ denotes the neutral part of the potential that acts on each ion from the walls and the nanoparticle. We find the equilibrium density profile $\rho_\alpha^0(\mathbf{r})$ that minimizes the free-energy functional $\Omega[\rho_\alpha(\mathbf{r})]$ through the variational derivative[53]

$$\left.\frac{\delta\Omega[\rho_\alpha(\mathbf{r})]}{\delta\rho_\alpha(\mathbf{r})}\right|_{\rho_\alpha^0} = 0 \tag{14}$$

At equilibrium, the associated grand potential free energy of the system is $\Omega^0 = \Omega[\rho_\alpha^0(\mathbf{r})]$.[54] The intrinsic Helmholtz free energy consists of four terms given by

$$F[\rho_\alpha(\mathbf{r})] = F_{\mathrm{id}}[\rho_\alpha(\mathbf{r})] + F_{\mathrm{hs}}[\rho_\alpha(\mathbf{r})] + F_{\mathrm{coul}}[\rho_\alpha(\mathbf{r})] + F_{\mathrm{corr}}[\rho_\alpha(\mathbf{r})] \tag{15}$$

The terms represent, respectively, the Helmholtz free energies for the ideal gas (id), hard spheres (hs), mean-field Coulombic interactions (coul), and second-order charge correlations (corr). The ion−ion correlation term F_{corr} in cDFT captures higher-order effects of density fluctuations, distinguishing the cDFT results from those of mean-field theories like the Poisson−Boltzmann (PB) theory. Further details are given in Section S.2, including the full form of the cDFT residual equations that we solve.

The residual equations are solved computationally within the spatial domain of the nanochannel. The cDFT calculations are performed using the open source package Tramonto, available at https://github.com/Tramonto/Tramonto. The residual equations are solved in real space on a Cartesian mesh using inexact Newton iterations for the density fields and a finite element method for the electrostatic potential. Details of these numerical methods and discussions of related applications of Tramonto to charged systems can be found in refs 55−58.

In the limit that the ions are treated as point particles and do not have any charge correlation contribution to their free energy, the cDFT reduces to the nonlinear Poisson−Boltzmann (PB) equation

$$\nabla^2\phi(\mathbf{r}) = -\frac{4\pi l_B}{d}\sum_\alpha \rho_\alpha^b \exp[-q_\alpha\phi(\mathbf{r})] \tag{16}$$

Here, d is a reference length in the system that for convenience we take to correspond to the ion size. The PB limit

DOI: 10.1021/acsomega.8b01393
ACS Omega 2018, 3, 11340−11353

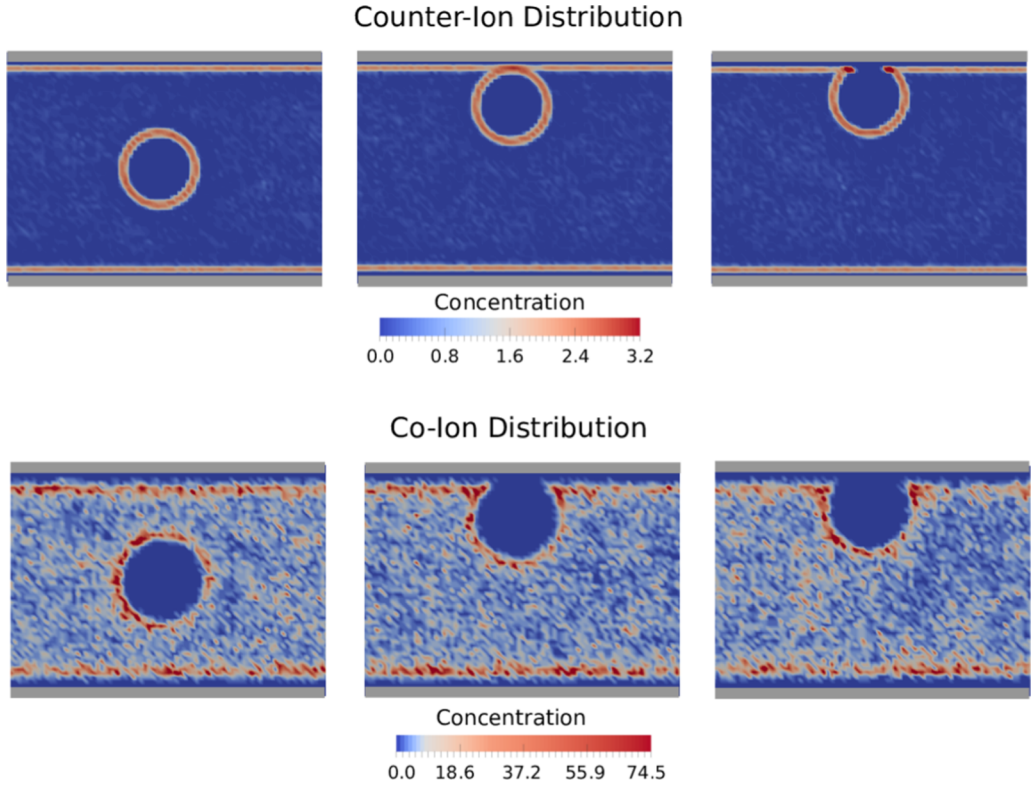

Figure 2. Average concentration of counterions (top) and coions (bottom) as the nanoparticle position is varied within the nanochannel, at $X_0^{(3)}$ = 3.0, 4.6, and 4.85 nm (left to right), for $\sigma = -3$ and $C_m = 8$. We also show the location of the channel walls (solid gray bars).

corresponds to the Helmholtz free-energy functional with only the ideal gas and mean-field Coulombic contributions.

2.2.1. Parameterization. We parameterized our cDFT calculations to yield results in physical regimes comparable to the BD simulations. We set the Bjerrum length l_B = 7.1 Å as in the simulations, use the same surface charge density on the nanoparticle, match the ion diameters $d = 2b$ = 0.232 nm, and use radius R = 0.75 nm for the nanoparticle. We used a channel with total width l_z = 6 nm as in the simulations. The channel walls extend into the channel to the same distance as in the simulations, so that we match the hard-wall condition in the density functional theory (DFT) with the Lennard-Jones 9-3 repulsive walls in the simulations.

To reduce computational costs in the cDFT calculations, we placed the nanoparticle with its center on the z axis so that the symmetry of the system allows for reflecting boundary conditions to be used in the x and y directions and thus only 1/4 of the particle needs to be directly included in the calculations. The size of the computational domain in the x and y directions was $l_x = l_y$ = 4.6 nm, for an effective channel length of 9.28 nm (taking into account the reflecting boundary through the center of the particle). We used a mesh size of 0.058 nm in all three-dimensional (3D) calculations (i.e., a mesh size of 0.25d in reduced units, where d = 0.232 nm is the diameter of the ions).

The BD simulations were performed in the canonical ensemble at constant N_α, V, and T. For cDFT, it is more natural to work in the grand canonical ensemble at constant μ_α,V, and T. To make a correspondence between these two sets of calculations, we set the chemical potentials in the cDFT so that the average ion densities match the BD simulations at the middle of the channel where nearly bulk conditions prevail. In the middle of the channel, the electrolyte solution is neutral, with $c_- = 2c_+$. We set the surface charge density of the channel walls in the cDFT equal to the effective surface charge densities given in Table 2.

We solve eqs S11−S13 in the nanochannel geometry with Neumann boundary conditions on $\phi(\mathbf{r})$ at the nanochannel walls and the nanoparticle, i.e., we set the charge density of these surfaces. We employ Dirichlet boundary conditions elsewhere, with a reflecting boundary through the nanoparticle, as described above.

To obtain the free energy associated with the particle at a particular position within the channel, we performed a cDFT calculation at each particle position and used the grand free energy of the resulting density. We computed density profiles of ions around the particle both in the case with the particle in the center of the channel and in the case with the particle in the bulk fluid with no channel present. The density profiles were found to be the same in both cases. We also found that the density profile near the channel wall, at a location in the channel far from the particle, was also independent of the presence or absence of the nanoparticle. This allowed us a significant reduction in computational costs by performing calculations of the wall density profiles from one-dimensional (1D) systems using cDFT. In our 1D calculations, we used a finer mesh size of 0.0232 nm for better resolution in the reported results.

3. RESULTS

We first discuss results of the BD simulations, followed by comparisons with cDFT and PB theory. All figures show results from the BD simulations unless explicitly noted otherwise.

3.1. Ionic Double-Layer Structure: BD Simulations. Typical distributions for the counterions and coions as the

DOI: 10.1021/acsomega.8b01393
ACS Omega 2018, 3, 11340−11353

nanoparticle position is varied in the case of $\sigma = -6$ and $C_m = 8$ are shown in Figure 2. For correspondence with continuum concentration fields, one must introduce a length scale over which we average the particle configurations to obtain a local notion of concentration. We report our concentration fields throughout in units of #/nm^3. In the regime with $\sigma = -6$ and $C_m = 8$, we see strong layering occurs for the counterions near the walls and near the nanoparticle surface. Also, a secondary layer of coions occurs offset from the walls and the nanoparticle surface adjacent to the counterion layer. This is especially visible for the coions shown in the bottom panel of Figure 2.

We show the ion concentrations near the wall for $\sigma = -6$ and varying C_m in Figure 3. The other cases with $\sigma = -1$ and

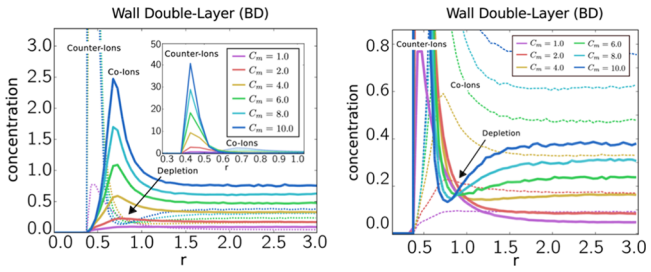

Figure 3. Ion concentrations near the channel walls as C_m is varied, for $\sigma = -6$. Left: density profiles for counterions (dashed curves) and coions (solid curves). Right: expanded scale with density profiles of counterions (solid curves) and coions (dashed curves). We remark that to help in comparing the data sets, we use throughout the figures in plots solid lines to help emphasize one ionic species and dotted lines to de-emphasize slightly the other ionic species against which we are making a comparison. To distinguish between the particular ionic species being plotted, we use labels embedded near the plots with the labels "counterions" or "coions." The distances r reported throughout are in units of nanometers. All concentrations are in units of #/nm^3.

-3 show ion concentrations that are indistinguishable after scaling the concentration in the case with $\sigma = -6$. For ions near the wall, there are two length scales associated with the ion layers. The first length scale is the location of the closest ion layer to the wall, which occurs at the minimum of the Lennard-Jones potential of eq 2, at $l_* = (18/45)^{1/6} b_w = 0.43$ nm. From the steric interactions, the next closest layer can form only around $l_2 = l_* + b_+ + b_-$. For the parameters in Table 1, we have $l_2 = 0.66$ nm. We see both of these length scales manifest in the structure of the ion layers. The double layer essentially forms according to the packing distance imposed by the ion and wall sterics. This becomes especially pronounced as the concentration increases, as seen in Figure 3.

As expected, as the ion concentration increases, the ion layers become smaller in width and more dense. For small concentrations, there is significant overlap between the counterion and coion layers with significant mixing of ions especially within the secondary coion layer. As the concentration increases, the layers become more distinct. For $C_m < 4$, the concentration of the counterions monotonically decays to the bulk counterion concentration, whereas for $C_m > 4$, the counterion density shows a depletion relative to the bulk density after the initial peak, as shown in the bottom of Figure 3. This charge oscillation is often seen for divalent counterions and strong surface charges, as in our system.[59,60]

In the nanochannel in the regimes, we consider the double-layer structure is markedly different than in weakly charged systems, which have an absorbed Stern layer of relatively immobile ions that transitions to a gaseous mobile phase of ions.[2,3] For our system, at high ion concentrations, this transition effectively occurs on the length scale of individual ions. Near the wall, the surface counterion and coion positions are strongly correlated, as shown in the simulation snapshot in Figure 4. Many of the ions form pairs with opposing ions or small clusters or chains. The wall surface is covered in a condensed layer of counterions along with a secondary layer of coions that forms as part of clusters near individual counterions; see Figure 4. This indicates some of the challenges involved in developing theory for such highly charged and concentrated regimes.

Next, we show the density of counterions and coions near the nanoparticle surface for the three different surface $\sigma = -1$, -3, and -6 in Figures 5, 6, and 7, respectively. The concentrations are measured at distances r relative to the nanoparticle surface. The relevant steric length scale for the position of the counterion layer in this case is the steric length $l_{**} = 2^{1/6}(R + b) - R = 0.22$ nm. The coion layer forms at a distance corresponding to $l_{2*} = l_{**} + 2b_{\pm} = 0.45$ nm. Again, the layer locations are primarily determined by the packing of the ions, as determined by the sterics.

For a relatively weak particle charge density of $\sigma = -1$, the counterions form a tight layer near the nanoparticle surface with significant mixing of coions into this primary layer. After this layer, the coions exhibit concentrations that rapidly approach the bulk; see Figure 5. For $\sigma = -3$, the counterions also form a tight layer near the nanoparticle surface but with

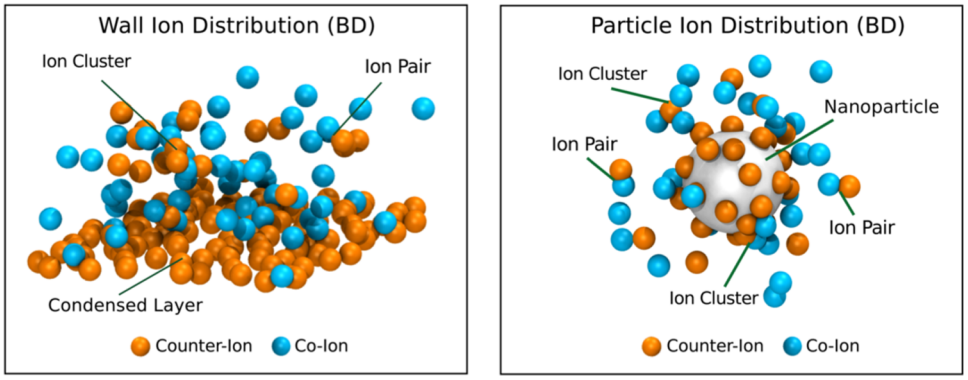

Figure 4. Left: ion configurations near the wall, for $\sigma = -6$ and $C_m = 8$. Right: ions near the nanoparticle in the bulk, for $\sigma = -6$ and $C_m = 8$, showing ion pairs and clusters.

DOI: 10.1021/acsomega.8b01393
ACS Omega 2018, 3, 11340−11353

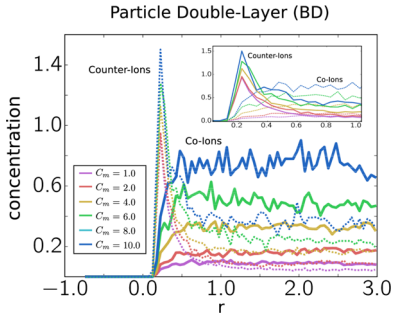

Figure 5. Nanoparticle double layer ($\sigma = -1.0$). We show as an inset a zoomed view of the layers over the range 0.0−1.0. We discuss related notational and plotting conventions in Figure 3.

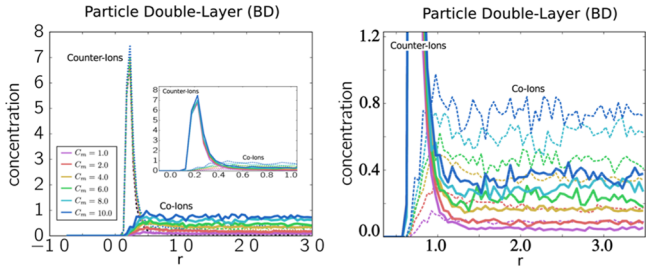

Figure 6. Nanoparticle double layer ($\sigma = -3.0$). We show as an inset a zoomed view of the layers over the range 0.0−1.0. We discuss related notational and plotting conventions in Figure 3.

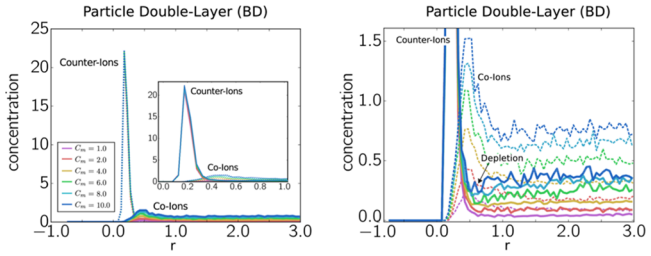

Figure 7. Nanoparticle double layer ($\sigma = -6.0$). We show as an inset a zoomed view of the layers over the range 0.0−1.0. We discuss related notational and plotting conventions in Figure 3.

relatively little mixing of coions into this primary layer; see Figure 6. The coions show only a weak secondary peak. For the highest surface charge density of $\sigma = -6$, a secondary layer of coions forms. For the largest concentrations, some depletion of the counterions is exhibited in the secondary layer relative to the bulk. This is less pronounced than in the case of the walls due to the high curvature of the particle but can be seen readily in the case with $\sigma = -6e/\text{nm}^2$ and $C_m = 10$, as highlighted in the inset in Figure 7.

For the smaller concentrations, there is significant overlap of the counterion layer with the coion layer, with significant mixing in the secondary layer. From examining configurations of the ions around the nanoparticle, we find this arises from strong correlations between the counterions and coions, resulting in the formation of transient charge clusters, as shown in Figure 4. As the nanoparticle charge increases, the layer of counterions near the particle adheres more strongly and the clusters are pushed increasingly toward the secondary layer. For the case $\sigma = -6$, this is especially pronounced with the double layer providing excess charge relative to what would be required to achieve local electric neutrality. We find the amount of excess charge increases monotonically with increasing bulk ion concentration; see Figure 8. Overcharging is often seen in systems with divalent counterions at sufficiently high concentrations and/or surface charges and is due to ion correlations.[50,61]

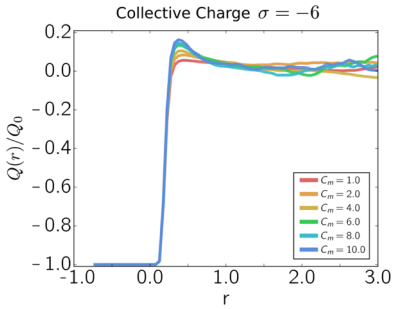

Figure 8. Total collective amount of charge $Q(r)$ contained within the spherical volume of radius r around the nanoparticle, for $\sigma = -6$. Near the particle surface, the double layer provides excess charges (overcharging) when countering the nanoparticle charge. Q_0 is the nanoparticle charge.

3.2. Free Energy of Nanoparticle Location: BD Simulations. We next consider the free energy $E(d)$ of the system as a function of the nanoparticle position d; see Figure 9. The wall and the nanoparticle are both negatively charged, so we expect the free energy to be repulsive when the particle is sufficiently close to the wall. As the concentration of the counterions and coions becomes sufficiently large, we find attraction occurs between the like-charged nanoparticle and wall. A free-energy minimum occurs at a distance comparable to the interaction length scale of the first layers of ions of the wall and the nanoparticle surface. This can be seen from the sum of the length scale for the first counterion layer of the wall $l_* = 0.43$ nm, and the length scale of the counterion layer of the nanoparticle $l_{**} = 0.22$ nm is $l = l_* + l_{**} = 0.65$ nm, corresponding to $\bar{d}/\frac{1}{2}L \sim 0.22$, the approximate location of the free-energy minima in Figure 9. The free-energy minimum can become significant compared to k_BT at sufficiently large C_m. We discuss this further in Section 4.

The free-energy profile has an interesting nonmonotonic dependence on the nanoparticle charge and electrolyte-ion concentrations. We see the depth of the free-energy minimum well that forms near the wall is not entirely monotonic as the ionic concentration increases. Most clearly, for $\sigma = -6$, the magnitude of the free-energy well depth is larger for $C_m = 6$ than for $C_m = 8$ but then increases significantly for $C_m = 10$. There is also a significant free-energy barrier, as large as $2k_BT$, that can arise separating the particle from the free-energy local minimum near the wall. Making this even more interesting is that the largest energy barriers appear to occur for the intermediate ionic concentrations considered. For instance, see the cases with $\sigma = -3$ and -6 and $C_m = 8$. The free-energy barrier appears to arise from the condensed ion layers that form on the nanoparticle surface and wall surface that must coordinate and rearrange as the particle approaches the wall; see Figure 10.

When the particle is at the free-energy minimum, the counterions in the condensed layer typically form transient ringlike structures near the surface of the nanoparticle, as shown in Figure 10. These counterions appear to serve double

DOI: 10.1021/acsomega.8b01393
ACS Omega 2018, 3, 11340−11353

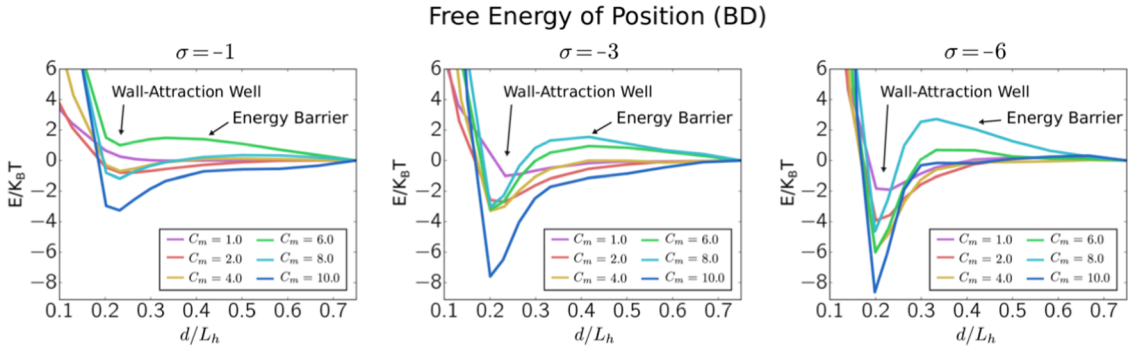

Figure 9. Free-energy profile of the nanoparticle−wall distance from BD simulations. We show the free energy for $\sigma = -1.0$, -3.0, and -6.0 as a function of the distance d between the particle and the wall. The results are normalized by the thermal energy k_BT and the half-width $L_h = \frac{1}{2}L$ of the nanochannel.

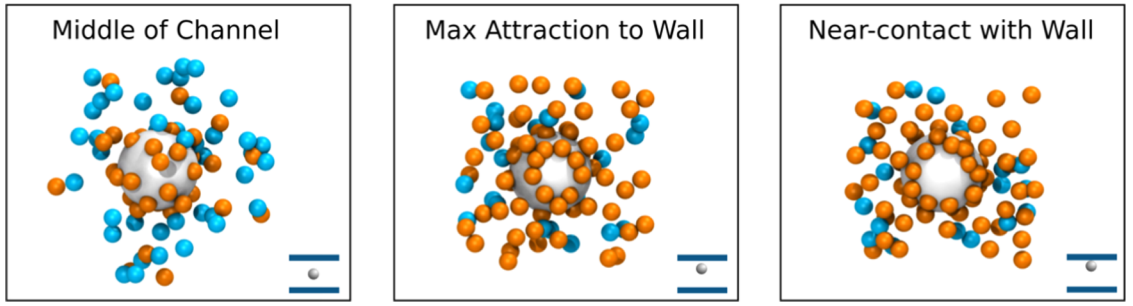

Figure 10. Top-down view of nanoparticle and ion distribution, showing typical distributions of ions nearby the nanoparticle at different locations within the nanochannel. We show the locations corrresponding to (i) the middle of the channel at $X_0^{(3)} = 3.0$ nm, (ii) the maximum attraction to the wall at $X_0^{(3)} = 4.6$ nm, and (iii) near-contact with the wall having large repulsion at $X_0^{(3)} = 4.85$ nm.

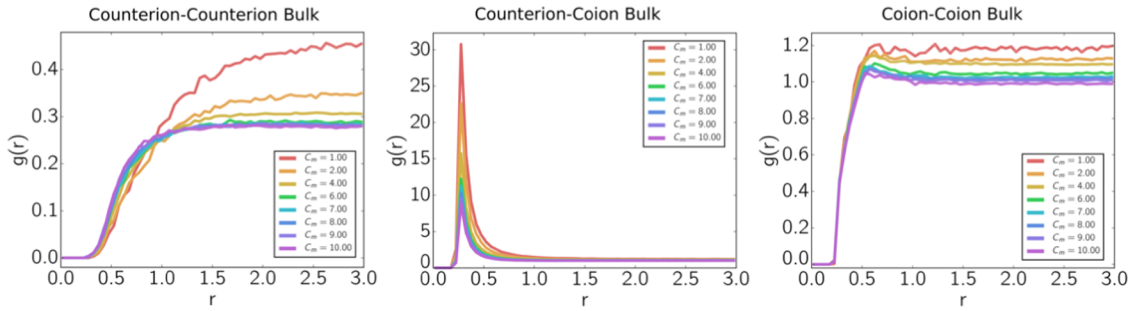

Figure 11. Radial distribution functions $g(r)$ for ion−ion correlations in the bulk from the BD simulations.

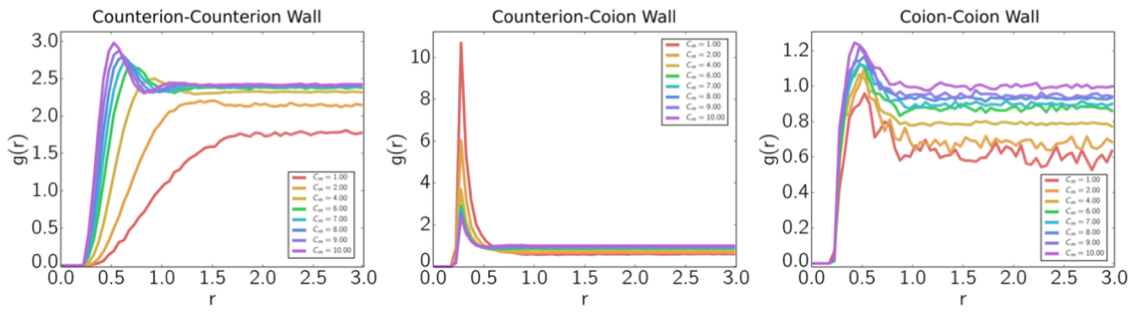

Figure 12. Radial distribution functions $g(r)$ for ion−ion correlations near the wall from the BD simulations.

duty in the condensed layer by screening both the nanoparticle charge and the effective wall charge. This double duty appears to be the source of the resulting free-energy gain. When the nanoparticle is positioned at an even closer distance to the wall, it penetrates into the condensed counterion layer. This excludes counterions, which results in a significant pressure on the nanoparticle surface, resulting in a strong free-energy penalty. It is important to remark that the effective electric field from the walls cancel so that all interactions beyond the steric distance are mediated by the ions.

DOI: 10.1021/acsomega.8b01393
ACS Omega 2018, 3, 11340−11353

3.3. Ion−Ion Correlations: BD Simulations. To further investigate the ion correlations in the system, we distinguish between two cases. The first case concerns those ion correlations that occur in the condensed layer near to the channel wall. The second case concerns the ion correlations that occur near the channel center. As a matter of convention, we refer to the ions near the channel wall as "wall" correlations and those near the center as being "bulk" correlations, as in Figures 11 and 12. We characterize the correlations by calculating a radial distribution function (RDF) $g(r)$ in two-dimensional for ions sampled within the condensed layer near the wall ($d < 1$ nm) and an (RDF) $g(r)$ in 3D for ions sampled in the bulk near the channel center ($d > 1$ nm); for more details see Section S.4. Here, d refers to the closest distance of the ion to the channel wall, in contrast, here, to the distance r measured from the reference ion in the RDF.

The RDFs $g(r)$ are normalized by the reference number concentration given by taking the count of all counterions or coions and dividing by the channel volume. Throughout our simulations, reference values are determined from the channel volume $V = 1944$ nm^3 and from the reference number concentrations $\hat{g}_- = 250/1944 \times C_m$ nm^{-3} and $\hat{g}_+ = 150/1944 \times C_m$ nm^{-3}. We remark that since the density of ions can be large near the walls, the $g(r)$ can exhibit long-range normalized bulk values that are significantly less than 1.0 and normalized wall values that are in excess of 1.0.

The RDFs in the bulk are shown in Figure 11. In the bulk, the counterion−counterion $g(r)$ shows a correlation hole, with the counterions not likely to be close together. The counterion−coion interactions show strong correlations that indicate a counterion has a cluster of coions in its proximity at a distance roughly twice the steric distance. The coion−coion $g(r)$'s exhibit a small feature around $r = 0.5$, which appears to be related to ionic clusters that form with multiple coions associated to a common counterion. Since we have divalent counterions, it makes sense that there should roughly be two coions associated with each counterion. These results indicate that on average, the bulk electrolyte consists of triples of ions with one counterion and two coions but not larger ion clusters.

Near to the wall, the RDF $g(r)$ exhibits features indicating much stronger correlations than those in the bulk. Although the counterion−coion correlations are similar to those in the bulk, the counterion−counterion $g(r)$ has a significant peak at small r. This is from the large density associated with the condensed counterion layer near the wall. As the charge increases, there is a transition around $C_m \geq 4$ from a correlated gaslike state to a state with significant correlations that are more liquidlike.[62] The peak that develops moves closer toward the steric length scale of the ions with peaks around 0.5 nm. The coion−coion correlations near the wall exhibit a peak for all of the regimes considered. From examining simulation trajectories, we find this arises from the strong correlations of the coions with the counterions and from bulk coions that transiently move to penetrate the strongly positively charged condensed layer. The coion−coion peak occurs independent of concentration around a similar length scale at 0.5 nm as the final counterion−counterion peaks for large concentration. These results show that there are some significant differences in ion−ion correlations when near the wall relative to the bulk.

3.4. Results from Classical Density Functional Theory (cDFT) and the Poisson−Boltzmann (PB) Theory. The classical density functional theory (cDFT) and Poisson−Boltzmann (PB) theory provide other approaches for investigating phenomena in electrolytes and charged systems that are expected to be more computationally efficient than BD simulations. However, in cDFT and PB, further approximations are incurred in modeling the underlying physics of the charged system. We expect that cDFT could provide a decent basis for describing the nanochannel system given the inclusion of terms accounting for charge correlations and ion sterics. The steric and correlation effects can be seen in the ionic layering and clustered interactions in the simulation results, particularly in Figures 1 and 4. To further emphasize the importance of these effects, we include in our comparisons the mean-field Poisson−Boltzmann (PB) theory, which we expect to be qualitatively incorrect in the strongly charged regime. These results further demonstrate the importance of ion correlation effects and sterics to obtain correct phenomenology even at a qualitative level.

We compare the ion densities near the channel walls as calculated from cDFT with the simulation density profiles in Figure 13. We find that cDFT predicts trends qualitatively

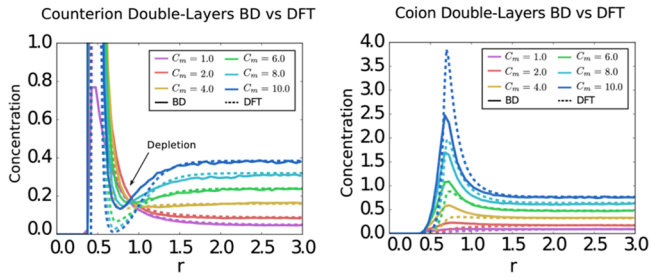

Figure 13. Left: comparison of the counterion densities for the cDFT (dashed curves) and BD simulations (solid curves) as a function of distance r from the channel wall, for wall charge densities from the $\sigma = -6$ column of Table 2. Right: comparison of the coion densities for the cDFT (dashed curves) and BD simulations (solid curves) as a function of distance r from the channel wall, for wall charge densities from the $\sigma = -6$ column of Table 2. We remark that in contrast to BD and cDFT, the mean-field PB theory would exhibit a monotonically varying density near the walls without such counterion depletion or coion enriched regions.

similar to the simulations but with some significant quantitative differences. At smaller values of C_m, the profiles exhibit monotonic behavior. As observed in the BD simulation results, at larger values of C_m, the cDFT counterion densities exhibit a distinct peak (condensed layer) followed by a depleted region before attaining the bulk counterion concentration; see Figure 13. The cDFT coion distributions exhibit a similar trend as in the BD results with a distinct peak occurring at the location of the depleted counterion region before attaining the bulk concentration; see Figure 13. The depletion after the first layer of counterions is not seen for ion densities calculated using the Poisson−Boltzmann equation nor for cDFT calculations with only mean-field electrostatics (i.e., without the correlation term F_{corr}). Instead, in the absence of ion correlations, the counterions exhibit a single peak near the wall that decays monotonically to the bulk whereas the coion density profiles simply increase monotonically from the wall to their bulk concentration, with no peak.

Thus, the cDFT charge correlation terms capture the charge density qualitatively as the ionic concentration is varied but as the system becomes more strongly charged, there are some significant quantitative deviations with the simulation results. Compared to the BD simulations, at smaller C_m, the cDFT

DOI: 10.1021/acsomega.8b01393
ACS Omega 2018, 3, 11340−11353

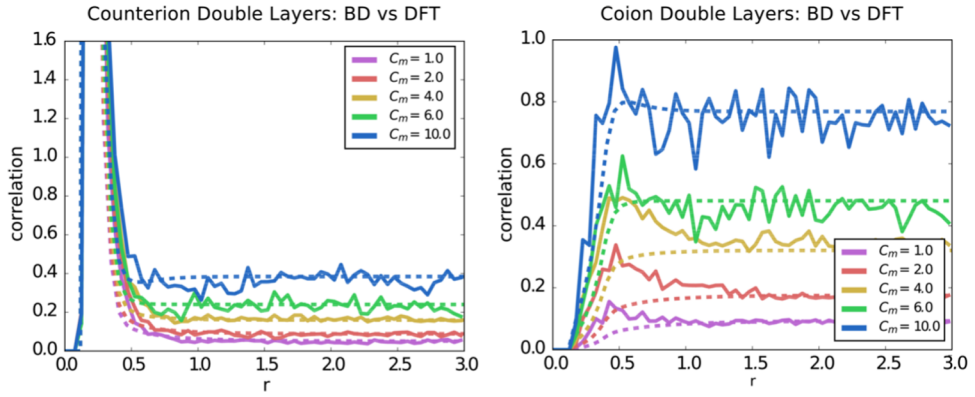

Figure 14. Left: comparison of the counterion densities for the cDFT (dashed curves) and BD simulations (solid curves) as a function of distance r from nanoparticle, for $\sigma = -3$. Right: Comparison of the coion densities for the cDFT (dashed curves) and BD simulations (solid curves) as a function of distance r from the nanoparticle, for $\sigma = -3$.

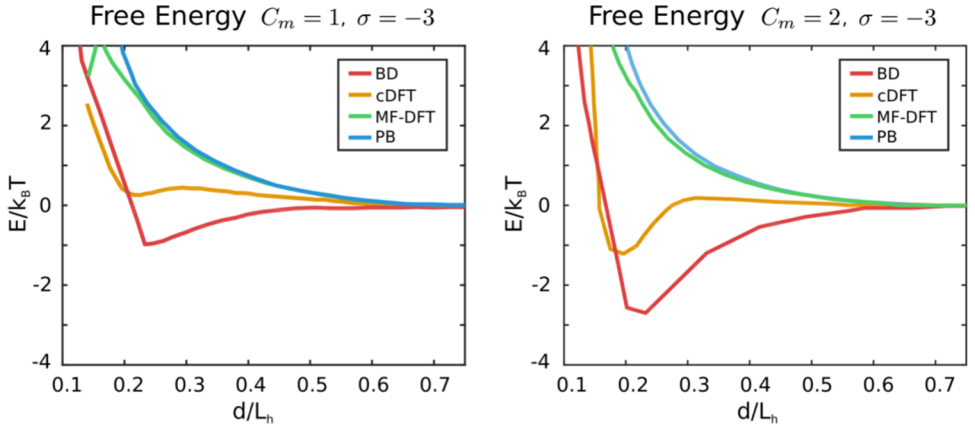

Figure 15. Comparison of the free energy as a function of particle position in the nanochannel for cDFT, mean-field cDFT, and PB theory with the BD simulations.

underestimates the magnitude of the coion peak but is in fairly good agreement with the long-range behavior of the counterion density profiles. At larger values, $C_m > 6$, the cDFT overestimates the magnitude of the coion peak and also overestimates the amount of depletion in the counterion density. For all concentrations and wall charge densities, the cDFT overestimates the counterion contact density at the charged wall as compared with the BD simulations (not shown).

Similar behavior is seen for the ion concentrations around the nanoparticle, as shown in Figure 14 for $\sigma = -3$. The cDFT underestimates the magnitude of the coion peak, especially for $C_m = 4$, and again overestimates the magnitude of the counterion contact density (not shown).

We note that we are using the simplest form of the charge correlation term in the cDFT, namely, the mean-spherical approximation (MSA) expression for the direct correlation function $c(r)$, evaluated at the bulk density of the ions (i.e., the densities in the middle of the channel). In our previous study of the interactions between charged nanoparticles in electrolyte, we found good agreement between cDFT and molecular dynamics (MD) simulations in the density profiles.[50] However, for our cDFT approach and for regimes comparable to our current studies, discrepancies have been previously observed with simulations having large ion concentrations and in regions near to highly charged walls in the work of Oleksy and Hansen.[51] Oleksy and Hansen compared cDFT to Monte Carlo simulations for a 1:1 electrolyte at 1 M concentration near a charged wall with reduced charge density $\sigma^* = 0.42$.[51] They also included a hard-sphere solvent and found differences in the ion density profiles of magnitude similar to those found in our work. Improvements to the charge correlation term, such as using the local weighted density in the calculation of $c(r)$, leads to excellent agreement between cDFT and, e.g., molecular dynamics (MD) simulations near highly charged surfaces.[63] The RFD functional of Gillespie and co-workers,[60] which uses a local weighted density in $c(r)$, has been shown to give good agreement with simulation results and experiment in a variety of studies.[60,64] Thus, in strongly charged regimes, a more sophisticated approach beyond the simple bulk MSA treatment is needed to capture ion correlations if quantitative accuracy is sought near surfaces. In this paper, our main focus was to gain further insight into the qualitative role of charge correlations so the more simple cDFT treatment is adequate. We also note that to our knowledge, more sophisticated treatments of charge correlations have not yet been implemented in a cDFT code that can also do 3D calculations in the geometry we study here.

Next, we consider the free energy for the nanoparticle as a function of position in the nanochannel. For systems with large ionic concentrations and high charge density on the particle, the cDFT becomes computationally difficult to converge given the localized structures that develop within the density fields. In Figure 15, we compare cDFT to the simulation results only

DOI: 10.1021/acsomega.8b01393
ACS Omega 2018, 3, 11340−11353

for $\sigma = -3$ and $C_m = 1.0$ and 2.0, values which are accessible with the cDFT computational methods. We see that cDFT captures the trends on a qualitative level compared to the simulation results. In particular, for sufficiently high charge, the cDFT also predicts the development of a free-energy minimum for the nanoparticle near the wall. In contrast, both the PB theory, which neglects sterics and correlations, and also mean-field cDFT with no charge correlations are found to predict a purely repulsive interaction energy between the nanoparticle and wall. Figure 16 shows cDFT results for differing charge densities on the nanoparticle, all at $C_m = 2.0$. As the charge on the particle increases, the depth of the minimum in the free energy increases, as also found (for higher particle charges) by the BD simulations. In some cases, the cDFT also predicts a small barrier in the free energy between the minimum and the center of the channel but with cDFT, we cannot access the high ion concentration regimes where this barrier is as large as that in the BD simulations.

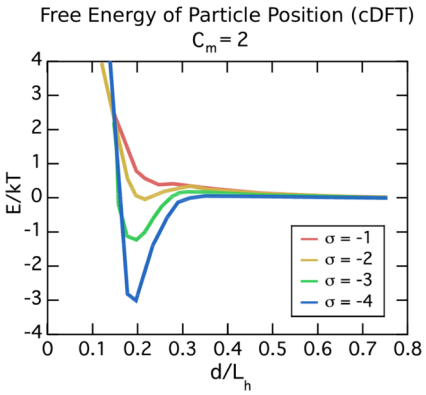

Figure 16. Free energy of the nanoparticle as a function of position from cDFT as the particle charge σ is varied.

The difficulty in converging the cDFT calculations was surprising, but the systems studied here have higher ion concentrations and surface charge densities than most previous cDFT studies. In particular, our previous investigation of the interactions between like-charged nanoparticles had maximum ion concentrations of about 220 mM, which is close to the smallest ion concentration in the current study.[50] Decreasing the strength of the electrostatic interactions slightly in the cDFT, by increasing the reduced temperature from $T^* = 0.33$ to 0.43 (where $T^* = d/l_B$), enabled convergence of systems with higher ion concentration (e.g., the $\sigma = -3$, $C_m = 4$ system). This change corresponds to increasing the ion diameter from 0.232 to 3.0 nm. However, further increases would be needed in T^* to get convergence at the higher ion concentrations so we did not pursue those calculations.

Although cDFT agrees qualitatively with the simulation results, there are some significant quantitative discrepancies. The location of the free-energy minimum in the cDFT is significantly closer to the nanochannel wall than the location of that in the BD simulations. This is likely due to the somewhat more narrow ion layers in the cDFT. We also find cDFT predicts a depth for the free-energy well that is significantly smaller than that observed in the simulation results; see Figures 15 and 16. Nevertheless, it is clear from these results that the attractive well results from ion charge correlations.

4. DISCUSSION

In the regimes studied, the ions tend to form clusters in the bulk electrolyte and a compact condensed layer near the channel walls. The interplay between the ionic layers associated with the nanoparticle and the wall can result in a significant attraction between the like-charged nanoparticle and wall. As discussed in Section 3.1, this occurs at a distance comparable to the thickness of the condensed counterion layer. As can be seen in Figures 3 and 7, there is a secondary layer of negative coions just beyond the counterion layer. At the distance of the free-energy minimum, the negatively charged nanoparticle joins the secondary layer of negative coions. From our comparisons between the BD simulations and cDFT calculations, we found the attraction to be a consequence of the ion−ion correlations. In contrast, the mean-field theories, either PB or mean-field cDFT, that neglect these correlations predict a purely repulsive interaction between the nanoparticle and wall.

The free energy of the nanoparticle location also exhibits an energy barrier. For the case of the strongly charged nanoparticle and ion concentrations ($\sigma = -6$ and $C_m = 8$), there is a significant condensed counterion layer on the particle surface. As the nanoparticle approaches the wall, the condensed layer of the nanoparticle merges with the condensed wall layer. These rearrangements in some charge regimes result in the free-energy barriers, as observed in Figure 9. This effect appears to occur only for intermediate ion concentrations of $C_m = 6$ and 8, for $\sigma = -3$ and -6, and disappears when the ion concentration becomes sufficiently large. The significant rearrangements that occur as the ion approaches the wall indicate a strong role played by the ion−ion correlations and discrete structures in determining the free energy of the wall−particle interactions.

It is interesting to consider further the differences between multivalent and monovalent systems. We performed two additional sets of simulations of monovalent systems with 1:1 electrolytes; further details and results are in Section S.3. In the first set of simulations, we keep the number density of the monovalent ions the same as that in the multivalent system. Although this case results in a different charge density, it retains the same entropic contributions in the free energy. In the second, we keep the charge density of the system the same but double the number of counterions, which increases the number of charge carriers and the entropic contributions in the free energy. In both cases, we find that the 1:1 electrolyte no longer results in a significant free-energy minimum. In the more strongly charged systems with more charge carriers, the free-energy minimum is further suppressed than in the case of the less charged system that shows a very small (relative to k_BT) and wide region of lower free energy; see Figures 9 and S1. This indicates that the multivalent system may benefit significantly from having fewer charge carriers, which reduces the entropic penalties associated with condensation of charge on the walls and strong correlations at the nanoparticle surface. There is also more of an energy gain or less entropic loss when sharing a screening charge in common. It can also be seen in the monovalent systems that the electrolyte is more diffused, without the presence of transient ion clusters as in the multivalent system. The simulation results indicate that it is the asymmetry between the ion charges and the reduced entropic penality for forming discrete structures that is responsible for the rich phenomena seen in multivalent electrolytes and

DOI: 10.1021/acsomega.8b01393
ACS Omega 2018, 3, 11340−11353

charged systems. It would also be of interest to explore how changing the channel width might affect double-layer structures and nanoparticle−wall interactions, especially in regimes where the two channel walls have double layers that strongly overlap.

Thus, the simulation results show that both the ion correlations and the resulting discrete ion configurations play important roles in determining the free energy of the system. In the BD simulations, strong electrostatic interactions and multivalent ions can result in the formation of discrete clusters and the interactions can be mediated at the level of individual ions and their arrangements, as seen in Figures 1, 4, and 10. This is expected to pose significant challenges in formulating constitutive equations for continuum descriptions of the system and in making quantitative predictions. The radial distribution functions we report for the counterions and coions for the bulk and near the wall may be helpful toward that aim; see Figures 11 and 12. The significant quantitative differences between the cDFT and the simulation results arise from the correlation terms in the cDFT functional that are based on the mean-spherical approximation (MSA) for bulk electrolytes. It would be of interest in future work to examine whether the RFD functional,[60] which is still based on the MSA direct correlation function but for the local (inhomogeneous) rather than bulk density, would be sufficient to match the present simulation results, or whether improved expressions for the direct correlation function, such as from the new DH-extended MSA (DHEMSA) closure of Olvera de la Cruz and co-workers,[65] would give better agreement. However, it may also be the case that for nanosystems with finite numbers of ions, finite ion numbers lead to effects that cannot be captured by density functional theories that by construction only include the average ion density.

5. CONCLUSIONS

We have investigated the behavior of a charged nanoparticle confined in a nanochannel. We have found for multivalent 2:1 electrolytes that strong ion−ion correlations can develop that give interesting free-energy profiles for the nanoparticle position within the channel. We found that the free-energy profile can exhibit minima giving a preferred location for the nanoparticle near the channel center and near to but separated from the channel wall. We found in some of the charge regimes, the minima can be separated by significant energy barriers. This is the result of overcharging of the double layer that forms near the nanoparticle surface, as seen in Figure 8. Comparisons between our BD simulations and cDFT and PB theory indicate the strong role played by ion−ion correlations. As may be expected from a mean-field theory, the PB theory was found to be inadequate in capturing even qualitative features of the simulation results. The cDFT approach is found to capture at a qualitative level the main trends seen in the simulation results both for the ionic densities and for the free-energy profile as the charge of the system is varied. However, the cDFT results have quantitative discrepancies with the simulation results, in both the ionic layer densities near the walls and in the depth of the free-energy well. This appears to arise from the MSA approach used for the charge correlation term, which is based on hard-sphere models of unconfined bulk electrolytes. Our simulations indicate that near surfaces, the ions can form interesting ionic structures, such as clusters or discrete layers differing significantly from bulk behaviors. To obtain more quantitative accuracy, such effects would have to be captured likely requiring further development of correlation terms for cDFT. Overall, the cDFT did make predictions in qualitative agreement with most of the BD simulation results.

The results, we report, could have implications for many phenomena within nanochannels and more broadly, nanodevices that rely upon electrical effects. For instance, in the case of capillary electrophoresis, the free-energy profile indicates that nanoparticles within the device may hop between positions close to the nanochannel wall and close to the channel center. Given the expected differences in particle mobilities in these locations, this could significantly affect arrival time observations. More generally, our results show that discrete ion−ion interactions may play a dominant role in nanodevices requiring more sophisticated theory than that provided by traditional mean-field approaches, such as the widely used Poisson−Boltzmann theory. Discrete ion effects could also lead to interesting depletion forces[66,67] between interacting nanoparticles or possibly in some regimes make contributions to the nanoparticle−wall interactions. The methods we have introduced here may be useful in performing further investigations of related depletion phenomena recently discussed in refs 68, 69. Toward the broader aim of developing better correlation terms for cDFT for charged systems, our bulk and wall radial distribution results may also be useful. Many of our results are expected to be useful in gaining insights into other charged systems such as biological macromolecules where similar discrete ion interactions and collective effects may be relevant.

■ ASSOCIATED CONTENT

Supporting Information

The Supporting Information is available free of charge on the ACS Publications website at DOI: 10.1021/acsomega.8b01393.

Analysis of electrostatics in channels; description of the classical DFT formulation; discussion of monovalent ion correlations; ion−ion correlation analysis methods (PDF)

■ AUTHOR INFORMATION

Corresponding Author

*E-mail: atzberg@gmail.com.

ORCID

Amalie L. Frischknecht: 0000-0003-2112-2587

Paul J. Atzberger: 0000-0001-6806-8069

Notes

The authors declare no competing financial interest.

■ ACKNOWLEDGMENTS

The authors P.J.A. and I.S.S. acknowledge support from research grant NSF CAREER DMS-0956210, NSF DMS—1616353, W. M. Keck Foundation, and DOE ASCR CM4 DE-SC0009254. We also acknowledge the UCSB Center for Scientific Computing NSF MRSEC (DMR-1121053) and UCSB MRL NSF CNS-0960316. The authors also thank Kai Sikorski for discussions and work for developing codes for LAMMPS. This work is supported by the Applied Mathematics Program within the Department of Energy (DOE) Office of Advanced Scientific Computing Research (ASCR) as part of the Collaboratory on Mathematics for

DOI: 10.1021/acsomega.8b01393
ACS Omega 2018, 3, 11340−11353

Mesoscopic Modeling of Materials (CM4). This work was performed, in part, at the Center for Integrated Nanotechnologies, an Office of Science User Facility operated for the U.S. Department of Energy (DOE), Office of Science. Sandia National Laboratories is a multimission laboratory managed and operated by National Technology and Engineering Solutions of Sandia, LLC., a wholly owned subsidiary of Honeywell International, Inc. for the U.S. Department of Energy's National Nuclear Security Administration under contract DE-NA0003525. This paper describes objective technical results and analysis. Any subjective views or opinions that might be expressed in the paper do not necessarily represent the views of the U.S. Department of Energy or the United States Government.

REFERENCES

(1) Squires, T. M.; Quake, S. R. *Rev. Mod. Phys.* **2005**, *77*, 977.
(2) Kirby, B. J. *Micro- and Nanoscale Fluid Mechanics: Transport in Microfluidic Devices*; Cambridge University Press: Cambridge, 2010.
(3) Bazant, M. Z. Induced-Charge Electrokinetic Phenomena. In *Electrokinetics and Electrohydrodynamics in Microsystems*; Ramos, A., Ed.; CISM Courses and Lectures; Springer: Vienna, 2011; Vol. *530*, pp 221−297.
(4) Derjaguin, B.; Landau, L. *Acta Physicochim. URSS* **1941**, *14*, 633−662.
(5) Verwey, E. J. W.; Overbeek, J. T. G. *Theory of the Stability of Lyophobic Colloids*; Elsevier: Amsterdam, 1948.
(6) Hansen, J. P.; Lowen, H. *Annu. Rev. Phys. Chem.* **2000**, *51*, 209−242.
(7) Pennathur, S.; Santiago, J. G. *Fluids Engineering Conference, ASME 2004 International Mechanical Engineering Congress and Exposition*, 2004; pp 191−196.
(8) Zänker, H.; Schierz, A. *Annu. Rev. Anal. Chem.* **2012**, *5*, 107−132.
(9) Kirby, B. J.; Hasselbrink, E. F. *Electrophoresis* **2004**, *25*, 187−202.
(10) Baker, N. A.; Sept, D.; Joseph, S.; Holst, M. J.; McCammon, J. A. *Proc. Natl. Acad. Sci.* **2001**, *98*, 10037−10041.
(11) Sun, H.; Wen, J.; Zhao, Y.; Li, B.; McCammon, J. A. *J. Chem. Phys.* **2015**, *143*, No. 243110.
(12) McCammon, J. A.; Harvey, S. C. *Dynamics of Proteins and Nucleic Acids*; Cambridge University Press: Cambridge, 1987.
(13) Baldessari, F. *J. Colloid Interface Sci.* **2008**, *325*, 526−538.
(14) Das, S.; Chakraborty, S. Implications of Interactions between Steric Effects and Electrical Double Layer Overlapping Phenomena on Electro-Chemical Transport in Narrow Fluidic Confinements. 2010, arXiv:1010.5731. arXiv.org e-Print archive. https://arxiv.org/abs/1010.5731 (accessed Oct 27, 2010).
(15) Guo, L.; Chen, S.; Robbins, M. O. *Eur. Phys. J.: Spec. Top.* **2016**, *225*, 1551−1582.
(16) Pegado, L.; Jönsson, B.; Wennerström, H. *J. Phys.: Condens. Matter* **2008**, *20*, No. 494235.
(17) Larsen, A. E.; Grier, D. G. *Nature* **1997**, *385*, 230−233.
(18) Moreira, A. G.; Netz, R. R. *Phys. Rev. Lett.* **2001**, *87*, No. 078301.
(19) Kanduč, M.; Naji, A.; Jho, Y. S.; Pincus, P. A.; Podgornik, R. *J. Phys.: Condens. Matter* **2009**, *21*, No. 424103.
(20) Kjellander, R.; Marčelja, S. *Chem. Phys. Lett.* **1984**, *112*, 49−53.
(21) Lau, A. W. C.; Lukatsky, D. B.; Pincus, P.; Safran, S. A. *Phys. Rev. E* **2002**, *65*, No. 051502.
(22) Sader, J. E.; Chan, D. Y. *J. Colloid Interface Sci.* **1999**, *213*, 268−269.
(23) Koltover, I.; Wagner, K.; Safinya, C. R. *Proc. Natl. Acad. Sci. U.S.A.* **2000**, *97*, 14046−14051.
(24) Stevens, M. J. *Biophys. J.* **2001**, *80*, 130−139.
(25) Schiessel, H.; Pincus, P. *Macromolecules* **1998**, *31*, 7953−7959.
(26) Kuron, M.; Arnold, A. *Eur. Phys. J. E: Soft Matter Biol. Phys.* **2015**, *38*, 20.
(27) Bloomfield, V. A. *Biopolymers* **1991**, *31*, 1471−1481.
(28) Nagornyak, E.; Yoo, H.; Pollack, G. H. *Soft Matter* **2009**, *5*, 3850−3857.
(29) Tagliazucchi, M.; Szleifer, I. *Mater. Today* **2015**, *18*, 131−142.
(30) Mojarad, N.; Krishnan, M. *Nat. Nanotechnol.* **2012**, *7*, 448.
(31) Gillespie, D. *J. Phys. Chem. B* **2010**, *114*, 4302−4309.
(32) Wan, Q.-H. *Anal. Chem.* **1997**, *69*, 361−363.
(33) Liu, Y.-W.; Pennathur, S.; Meinhart, C. D. *J. Colloid Interface Sci.* **2016**, *461*, 32−38.
(34) Liu, Y.-W.; Pennathur, S.; Meinhart, C. D. *Phys. Fluids* **2014**, *26*, No. 112002.
(35) Torrie, G.; Valleau, J. *Chem. Phys. Lett.* **1979**, *65*, 343−346.
(36) Valleau, J. P.; Cohen, L. K.; Card, D. N. *J. Chem. Phys.* **1980**, *72*, 5942−5954.
(37) Valleau, J. P.; Cohen, L. K. *J. Chem. Phys.* **1980**, *72*, 5935−5941.
(38) Weeks, J. D.; Chandler, D.; Andersen, H. C. *J. Chem. Phys.* **1971**, *54*, 5237−5247.
(39) Griffiths, D. J. *Introduction to Electrodynamics*, 3rd ed.; Prentice Hall: Upper Saddle River, New Jersey, 1999.
(40) Hockney, R. W.; Eastwood, J. W. *Computer Simulation Using Particles*; Taylor & Francis Group: New York, 1988.
(41) Pollock, E.; Glosli, J. *Comput. Phys. Commun.* **1996**, *95*, 93−110.
(42) Plimpton, S. *J. Comput. Phys.* **1995**, *117*, 1−19.
(43) Yeh, I.-C.; Berkowitz, M. L. *J. Chem. Phys.* **1999**, *111*, 3155−3162.
(44) Ballenegger, V.; Arnold, A.; Cerdà, J. J. *J. Chem. Phys.* **2009**, *131*, No. 094107.
(45) Gardiner, C. W. *Handbook of Stochastic Methods*, 3rd ed.; Series in Synergetics; Springer: Berlin, 1985.
(46) Wang, Y.; Sigurdsson, J.; Atzberger, P. *SIAM J. Sci. Comput.* **2016**, *38*, S62−S77.
(47) Moreira, A. G.; Netz, R. R. *Europhys. Lett.* **2000**, *52*, 705.
(48) Allahyarov, E.; D'Amico, I.; Lowen, H. *Phys. Rev. Lett.* **1998**, *81*, 1334−1337.
(49) Grønbech-Jensen, N.; Beardmore, K. M.; Pincus, P. *Phys. A* **1998**, *261*, 74−81.
(50) Salerno, K. M.; Frischknecht, A. L.; Stevens, M. J. *J. Phys. Chem. B* **2016**, *120*, 5927−5937.
(51) Oleksy, A.; Hansen, J.-P. *Mol. Phys.* **2006**, *104*, 2871−2883.
(52) Henderson, D.; Lamperski, S.; Jin, Z.; Wu, J. Z. *J. Phys. Chem. B* **2011**, *115*, 12911−12914.
(53) Gelfand, I. M.; Fomin, S. V. *Calculus of Variations*; Dover: NY, 2000.
(54) Evans, R. *Adv. Phys.* **1979**, *28*, 143−200.
(55) Frink, L. J. D.; Salinger, A. G.; Sears, M. P.; Weinhold, J. D.; Frischknecht, A. L. *J. Phys.: Condens. Matter* **2002**, *14*, 12167.
(56) Heroux, M. A.; Salinger, A. G.; Frink, L. J. D. *SIAM J. Sci. Comput.* **2007**, *29*, 2059−2077.
(57) Muller, R. P.; Cygan, R. T.; Deng, J.; Frischknecht, A. L.; Hewson, J. C.; Kanouff, M. P.; Larson, R.; Moffat, H. K.; Tenney, C. M.; Schultz, P. A.; Wagner, G. J. *Modeling Thermal Abuse in Transportation Batteries*; Technical Report No. SAND2012-7816; Sandia National Laboratories: Albuquerque, 2012.
(58) Frink, L. J. D.; Frischknecht, A. L.; Heroux, M. A.; Parks, M. L.; Salinger, A. G. *J. Chem. Theory Comput.* **2012**, *8*, 1393−1408.
(59) Boda, D.; Fawcett, W.; Henderson, D.; Sokolowski, S. *J. Chem. Phys.* **2002**, *116*, 7170−7176.
(60) Gillespie, D.; Valiskó, M.; Boda, D. *J. Phys.: Condens. Matter* **2005**, *17*, 6609.
(61) Yu, Y. X.; Wu, J. Z.; Gao, G. H. *J. Chem. Phys.* **2004**, *120*, 7223−7233.
(62) Chandler, D. *Introduction to Modern Statistical Mechanics*; Oxford: New York, 1987.
(63) Lee, J. W.; Nilson, R. H.; Templeton, J. A.; Griffiths, S. K.; Kung, A.; Wong, B. M. *J. Chem. Theory Comput.* **2012**, *8*, 2012−2022.
(64) Gillespie, D.; Khair, A. S.; Bardhan, J. P.; Pennathur, S. *J. Colloid Interface Sci.* **2011**, *359*, 520−529.

DOI: 10.1021/acsomega.8b01393
ACS Omega 2018, 3, 11340−11353

(65) Zwanikken, J. W.; Jha, P. K.; de la Cruz, M. O. *J. Chem. Phys.* **2011**, *135*, No. 064106.
(66) Asakura, S.; Oosawa, F. *J. Polym. Sci.* **1958**, *33*, 183−192.
(67) Asakura, S.; Oosawa, F. *J. Chem. Phys.* **1954**, *22*, 1255−1256.
(68) Moazzami-Gudarzi, M.; Maroni, P.; Borkovec, M.; Trefalt, G. *Soft Matter* **2017**, *13*, 3284−3295.
(69) Zeng, Y.; Grandner, S.; Oliveira, C. L. P.; Thünemann, A. F.; Paris, O.; Pedersen, J. S.; Klapp, S. H. L.; von Klitzing, R. *Soft Matter* **2011**, *7*, 10899−10909.

DOI: 10.1021/acsomega.8b01393
ACS Omega 2018, 3, 11340−11353